

Exploring SIMPLE algorithm for all speeds

M.M. Rahman*, Wenchang Liu, Ming Lv, Huachen Pan*

Hangzhou Dianzi University, School of Mechanical Engineering, 310018 Hangzhou, China

ARTICLE INFO

Article history:

Received 18 August 2021

Revised 13 March 2022

Accepted 20 May 2022

Available online 07 June 2022

Keywords:

SIMPLE algorithm

Under-relaxation

Compressibility

Diagonal dominance

Convergence and robustness

ABSTRACT

The segregated SIMPLE algorithm is developed on a curvilinear collocated grid using a cell-centered finite-volume Δ -formulation to speculate all-speed fluid flows. The occurrence of velocity-pressure decoupling is unraveled by invoking a consistently formulated dual-dissipation scheme. A modified flux-difference scheme calculates viscous fluxes at all speeds. A local Mach number based indicator is initiated to impose a constraint on the actual state of compressibility, related to the density-updating in the corrector step of SIMPLE algorithm. The positivity in influence coefficients' diagonal-dominance with the corrector step is guaranteed by the current contrivance, preventing the need for an under-relaxation (UR) factor. For a selected low Mach number flow, comparisons reveal the relevance of incompressible approach, sprung from the unique compressible solver.

© 2022 THE AUTHORS. Published by Elsevier BV on behalf of Faculty of Engineering, Ain Shams University. This is an open access article under the CC BY license (<http://creativecommons.org/licenses/by/4.0/>).

1. Introduction

To predict flows at all Mach numbers, much attention is paid to develop the pressure-based SIMPLE (Semi-Implicit Method for Pressure Linked Equation) algorithm and its deviants. The sound speed C in this situation has an appreciable influence on determining a plausible success [1–4] and resorting to a delimiting aspect to this development, the incompressibility is recaptured. Discretized continuity and momentum equations [5] are applied to derive the SIMPLE algorithmic pressure-correction equation (PCE); the density is replaced by the pressure for compressible flows using an appropriate equation of state (EOS). The characteristic PCE is hyperbolic in the supersonic region and elliptic in the subsonic flow region, provided that the transition from supersonic to subsonic flow must be appreciably smoothed with included compressibility effects [1]. Generally, when compressible-flow simulations involve the PCE, the evaluation of density is switched on after the establishment of a sensible pressure field (after a certain number of iterations). An upwind treatment of density in the pressure-correction reduces the stability [4] and a check has to be performed

to justify the diagonal dominance of influence coefficients which is not always ensured due to the fact that volumetric in and out flows may not be equal [1,3]. Once the corrected pressure field is available, density and velocity fields are updated to compensate the continuity constraint. It must be stressed herein that the SIMPLE imitates the artifacts of preconditioned density-based compressible methods [6,7] and thus, inheriting a admissible foundation to expand its potentiality regarding all-speed fluid flows. Nonetheless, the physical requirement of SIMPLE on a collocated grid is to eradicate the decouplings of pressure-density and pressure-velocity fields. To eliminate destabilizing effects originating from the decoupling phenomena, many novel primitive-variable based formulations have been devised on collocated grid arrangements [8–11].

Ong and Chan [12] have developed a pressure-based Mach-uniform method by combining the “Simple Low-dissipation Advection Upstream Splitting Method” (SLAUPM) numerical scheme and the higher temporal order pressure-based algorithm. This hybrid scheme avoids the limitation of SLAUPM in the low-Mach number regime as well as deficiencies of the pressure-based method in the high-Mach number regime. The Rhie-Chow momentum interpolation scheme has been modified for accurate shock-capturing and computing subsonic flows without empirical scaling of numerical dissipation at low-Mach number. However, the current work has extended the SIMPLE algorithm for all Mach-number flows, details of which are given subsequently. The SIMPLE Algorithm is an implicit pressure-based scheme for Navier-Stokes equations. Efficient and iterative solvers have been well-developed based on the SIMPLE Algorithm within the framework of finite-volume

* Corresponding authors.

E-mail addresses: mizanur_rahman@hdu.edu.cn (M.M. Rahman), huachen_pan@hdu.edu.cn (H. Pan).

Peer review under responsibility of Ain Shams University.



Production and hosting by Elsevier

method, achieving the well-accepted applicability due to the fact that mass, momentum and energy are conserved even on coarse grids [13].

The current research embraces fluid flow problems with two-dimensional (2-D) identity using a fully collocated cell-centered finite-volume method, encompassing the entire spectrum of subsonic to hypersonic flows. The system of equations is solved with a segregated manner, sticking to convergence based on diagonal dominance. The present formulation has several desirable attributes relative to the conventional all-speed computable SIMPLE algorithm: (a) it provides a new insight into the influence coefficients since the discretized PCE has a close resemblance to those of momentum and scalar equations; (b) non-physical oscillations due to the pressure-velocity decoupling are alleviated, employing a compatible cell-face dissipation scheme [10,11]; (c) the inclusion of discrete time-derivative of pressure-correction (e.g., $\partial p/\partial t \approx p'/\Delta t$) with the enthalpy equation enforces a consistent energy balance, resulting in a coupling between them; (d) the change in density that can be interpreted physically as contributions from the specific enthalpy change and the advection of pressure-correction is added with the fictitious mass imbalance to meet the net mass imbalance for compressible flow; (e) the fictitious mass imbalance is calculated using the Newton-type linearization in favor of an amended cell-face dissipation approach and a TVD (total variation diminishing) slope limiter, accounting for an enhanced solution stability; (f) Rusanov flux-difference scheme [14] is reconstructed to evaluate viscous fluxes at all flow speeds; (g) a local Mach number based indicator determines the appropriate state of compressibility adhering to the density-updating in the corrector step and finally (h) the current solver avoids the switching on/off regulation in the density evaluation and ensures the positivity in the diagonal dominance of SIMPLE corrector-step equation. The inclusive architecture greatly facilitates an avoidance of under-relaxation (UR) and enhances the convergence. To substantiate the accuracy and efficacy of proposed SIMPLE algorithm, a few well-documented numerical experiments are considered: a buoyancy-driven cavity flow [15], shock-tube problems [16,17] and flow around an airfoil.

2. Equations of motion

With the Einstein notation, incompressible/compressible flow equations consisting of continuity, momentum and energy can be given as follows:

$$\frac{\partial \rho}{\partial t} + \frac{\partial \rho u_i}{\partial x_i} = 0 \quad (1)$$

$$\frac{\partial \rho u_i}{\partial t} + \frac{\partial \rho u_i u_j}{\partial x_j} + \frac{\partial p}{\partial x_i} = \frac{\partial \tau_{ij}}{\partial x_j} \quad (2)$$

$$\frac{\partial \rho E}{\partial t} + \frac{\partial \rho u_j H}{\partial x_j} = \frac{\partial u_i \tau_{ij}}{\partial x_j} - \frac{\partial q_j}{\partial x_j} \quad (3)$$

$$\frac{\partial \rho H}{\partial t} = \frac{\partial \rho E}{\partial t} + \frac{\partial p}{\partial t} \quad (4)$$

where ρ the density, u_i the velocity vector, t the time, x_i the Cartesian coordinates, τ_{ij} the viscous stress tensor, p the pressure and q_j the j -directional heat-flux component. The total internal energy and enthalpy are $E = e + u_i^2/2$ and $H = E + p/\rho = h + u_i^2/2$, respectively. The specific internal energy and enthalpy are $e = c_p T$ and $h = c_p T$, respectively; T is the temperature. The specific heat capacity at a constant pressure is c_p and the specific heat capacity at a constant volume is c_v . The heat conductivity λ can be calculated from the relation $\lambda = \mu c_p / Pr$, where Pr and μ are the Prandtl number and dynamic viscosity, respectively. The heat flux is determined from $\mathbf{q} = -\lambda \nabla T$. The enthalpy Eq. (4) is preferred to convoke the impact of pressure-correction p' on the energy equation; since no lineariza-

tion is required by the transient pressure term, the formulation is straightforward. An appropriate EOS can close the system of governing equations; the perfect gas replica provides state variables as follows:

$$C = \sqrt{\frac{\gamma p}{\rho}} = \sqrt{\gamma R T}, \quad \rho = \frac{\gamma p}{(\gamma - 1)h} = \frac{\gamma p}{(\gamma - 1)c_p T}, \quad H = E + \frac{p}{\rho} = \frac{C^2}{\gamma - 1} + \frac{u_i^2}{2} \quad (5)$$

where $c_p = \gamma R/(\gamma - 1)$, R implies the universal gas constant and $\gamma = c_p/c_v$ is the ratio of specific heat capacities and C signifies the real sound speed. Typically $\gamma = 1.4$ and $R = 287 \text{ J/kg} \cdot \text{K}$ for air; absolute magnitudes of the thermodynamic pressure and temperature must be considered when evaluating other thermodynamic state parameters using an EOS.

In practice, the non-conservative form of continuity equation involves a $\partial p'/\partial t$ (time-derivative of pressure-correction) in order to accelerate an avoidance of UR factors [6,7] associated with the SIMPLE algorithm for an incompressible flow. This is a vital approach to reviving an artificial sound (or pseudo-sound) speed \tilde{C} ; it is crucial for augmenting the solver convergence to the steady-state by disregarding a UR factor. Relaxing the incompressibility constraint, the steady mass continuity can be perturbed; applying the chain rule to a 2-D framework provides:

$$\frac{\partial \rho'}{\partial p'} \frac{\partial p'}{\partial t} + \rho \left(\frac{\partial u}{\partial x} + \frac{\partial v}{\partial y} \right) = 0 \quad (6)$$

Readjusting Eq. (6) yields:

$$\frac{1}{\tilde{C}^2} \frac{\partial p'}{\partial t} + \rho \left(\frac{\partial u}{\partial x} + \frac{\partial v}{\partial y} \right) = 0 \quad (7)$$

where the parameter \tilde{C} is potentially defined by:

$$\frac{1}{\tilde{C}^2} = \frac{\partial \rho'}{\partial p'} \quad (8)$$

and \tilde{C} is determined with a numerical optimization as:

$$\tilde{C} = \beta \sqrt{\max \left[(u^2 + v^2); \frac{1}{2} U_r^2 \right]} \quad (9)$$

where U_r implies a reference velocity and β indicates a compressibility parameter which influences the pseudo-sound speed \tilde{C} substantially, affecting the solver convergence and stability significantly [18,19]. With a local Mach number $M_l = (|u|, |v|)/C \leq 0.3$ as evaluated by a thumb-rule [20], the compressible flow conserves the incompressibility-limit. Accordingly, a value of $\beta \approx 3.0$ is suggested to accommodate better convergence at the steady-state by enforcing the mass conservation; it can be ensured that even at stagnation points, \tilde{C} reaches a non-zero value. Nevertheless, the local sound speed must be bounded since both incompressible and compressible solvers share the same modeling approach:

$$C = \min \left(\sqrt{\gamma p/\rho}; \tilde{C} \right) \quad (10)$$

Clearly, the actual local sound speed $C = \sqrt{\gamma p/\rho}$ prevails over \tilde{C} when $M_l \geq 0.3$. Note that U_r may not be available with some compressible flows, however, a reference sound speed C_r is procurable; it is relevant to set $U_r = C_r$ in this situation. Conservative variables of continuity, momentum and energy equations can be denoted by $W = (\rho, \rho u, \rho v, \rho H)^T$. Governing equations are formulated as conservative and solved for primitive variables u_i^* and H ; tentative velocity u_i^* and pressure p^* fields are afterward corrected by the SIMPLE method. As primary solution variables retain a consistent

discretization [8], conservative properties of the system of equations remain unaffected using primitive solution variables instead of conserved variables. When solving incompressible flows, no approximations are introduced with governing equations although the impact of some terms may become insignificant in Eqs. (1)–(4). The solver utilizes a pressure-difference $\Delta p = p - p_\infty$ since it is also applied to an incompressible flow. Nevertheless, the energy flux must use the absolute pressure p ; the addition of constant ambient pressure p_∞ with the interpolated Δp yields an absolute pressure.

3. Spatial -discretization

The energy equation together with 2-D Navier-Stokes equations is solved using a cell-centered finite-volume method, leading to the following integral relation:

$$\frac{d}{dt} \int_V W dV + \int_S \vec{F}(W) \cdot d\vec{S} = \int_V f dV \quad (11)$$

for a boundary S with a region V ; conservative variables $W = (\rho, \rho u, \rho v, \rho H)^T$ and the source term is indicated by f . Integration for a computational cell i results in:

$$\forall_i \frac{dW_i}{dt} = \sum_{\text{faces}} -\vec{S}\vec{F} + \forall_i f_i \quad (12)$$

where the sum accords with computational cell faces. The unit normal vector \vec{n} corresponding to each cell face can be given by

$$\vec{n} = n_x \vec{i} + n_y \vec{j} = \frac{S_x}{S} \vec{i} + \frac{S_y}{S} \vec{j} \quad (13)$$

and the correlated aspect for cell-face flux matches

$$\hat{F} = n_x F + n_y G \quad (14)$$

where F and G are associated with Eqs. (1)–(3), representing inviscid and viscous fluxes in the x and y directions, respectively. Viscous fluxes can be computed in a straightforward manner; a second-order central-difference scheme with the thin-layer approximation is utilized to calculate viscous fluxes on a non-orthogonal grid. Primitive variables $\tilde{W} = (u, v, H)^T$ are determined with Van Leer's MUSCL (monotone upstream-centered schemes for conservation laws) approach [21] to calculate the inviscid flux on the cell-face ($i + 1/2$). In order to take an account of directional impacts upon upwinding schemes [7], a rotational matrix is employed to evaluate inviscid fluxes at the cell face. The conversion of contravariant momentum-flux components to primitive ones is induced by the rotational matrix, resembling the flux components encountered in a Cartesian-coordinate system.

For compressible flows, several flux-difference and flux-vector splitting approaches are obtainable from the literature. Presumably, the most simplest alternative is the Rusanov approach [14] which can be formulated on the cell-face ($i + 1/2$) as

$$\hat{F}_{i+1/2} = \frac{1}{2} \left[F(W_{i+1/2}^R) + F(W_{i+1/2}^L) - a_{i+1/2} (W_{i+1/2}^R - W_{i+1/2}^L) \right] \quad (15)$$

where $a_{i+1/2} = |U| + C$ is the spectral radius of Jacobian flux on the cell-face; it is the maximum magnitude of eigenvalue, adhering to the Jacobian flux and $U = un_x + vn_y$ signifies the contravariant velocity component. The cell-face mass flux ρU with the predictor step of SIMPLE is approximated using an averaging between neighboring nodal points and ρU can be manipulated as a dissipation scaling. Therefore, Eq. (15) can be modified as

$$\hat{F}_{i+1/2} = \frac{1}{2} \left[\rho U (\tilde{W}^R + \tilde{W}^L) - |\rho U| (\tilde{W}^R - \tilde{W}^L) \right]_{i+1/2} \quad (16)$$

In other words, the spectral radius is tuned with a view to avoiding immoderate dissipation when calculating inviscid fluxes of the momentum and scalar, especially at low-Mach number flows.

3.1. Cell-face velocity and pressure

A cell-face dual-dissipation approach is used to get rid of the pressure-velocity decoupling on a collocated grid [10,11]; the overall scheme is amended, convoking explicit reconstructions into the cell-face pressure and velocity as follows:

$$p_{i+1/2} = \bar{p}_{i+1/2} - \frac{\rho_{i+1/2}}{4\beta} |U^R + U^L| (U^R - U^L) \quad (17)$$

$$U_{i+1/2}^* = \bar{U}_{i+1/2} - \frac{\Delta n_{i+1/2}}{4} \left(\frac{1}{(\rho C)_{i+1}} - \frac{1}{(\rho C)_i} \right) (f_{i+1} - f_i) - \left(\frac{1}{2\rho C} \right)_{i+1/2} (p^R - p^L) \quad (18)$$

where the superscript asterisk on U denotes a tentative value and the significance of 'overbar' is an averaging between neighboring nodal points; a distance between cell centers is indicated by $\Delta n_{i+1/2} = (\forall_i + \forall_{i+1})/2$ and $f = f_x n_x + f_y n_y$. The $(p, U)_L$ and $(p, U)_R$ are respective state variables on left and right sides of the cell-face; they are approximated with a fully upwinded second-order (FUS) approach. Since both velocity and pressure are mutually connected to adjoining grid nodes, Eqs. (17 and 18) account for a strong coupling between velocity and pressure, giving rise to a cell-face interpolation method with non-linear characteristics. Noteworthy, Eq. (17) determines the momentum-equation cell-face pressures and Eq. (18) is utilized to compute tentative cell-face velocities, forming the mass imbalance for the PCE.

3.2. SIMPLE-predictor step

Conservative explicit residuals are transformed to primitive residuals prior to the implicit phase; this transformation represents an explicit fluid constitutive correlation which can be cast in a matrix form:

$$\begin{pmatrix} \Delta \rho \\ \Delta u \\ \Delta v \\ \Delta H \end{pmatrix} = \frac{1}{\rho} \begin{pmatrix} \rho & 0 & 0 & 0 \\ -u & 1 & 0 & 0 \\ -v & 0 & 1 & 0 \\ -H & 0 & 0 & 1 \end{pmatrix} \begin{pmatrix} \Delta \rho \\ \Delta \rho u \\ \Delta \rho v \\ \Delta \rho H \end{pmatrix} \quad (19)$$

Conservative explicit residuals ΔW can be readily procured from:

$$\Delta W = (\Delta \rho, \Delta \rho u, \Delta \rho v, \Delta \rho H)^T = \frac{\Delta t_i}{\forall_i} R_i \quad (20)$$

where residuals R_i are calculated from the RHS of Eq. (12) and the spatially varying pseudo-time step Δt_i is estimated from Reference [6]. The operation comes across an explicit density residual $\Delta \rho$ with an equivalence to the mass source formed by renovated velocity (and density) fields; this mass imbalance is perhaps conducive to linearizing conservative residuals and predicting a realistic pressure field by avoiding the UR factor.

It is worth pointing out that the primitive explicit specific enthalpy and temperature residuals are calculated as follows:

$$\begin{aligned} \Delta \rho H &= \Delta \rho E + p^n \\ \Delta H &= \frac{1}{\rho} (\Delta \rho H - H \Delta \rho) \\ \Delta h &= \Delta H - u \Delta u - v \Delta v \\ \Delta T &= \Delta h / c_p \end{aligned} \quad (21)$$

where p^n in Eq. (21) is the pressure-correction from the previous iteration, maintaining a coupling between the energy equation

and PCE. This coupling is usually frozen and the discretized specific internal energy equation is exploited to recover an algebraic equation for the specific enthalpy change Δh [4], resulting in an explicit introduction of UR factors with pressure-velocity corrections.

The implicit pseudo-time integrated Eq. (12) with a first-order backward differencing to temporal variations of \tilde{W}_i provides a discretized system of algebraic equations, accompanying a partial factorization in the presence of a source term [7]:

$$\left[1 - \Delta t_i \frac{\partial f}{\partial W_i}\right] \Delta \tilde{W}_i^* = \Delta \tilde{W}_i^{**} \quad (22)$$

$$\left[1 + \xi \left|\frac{\Delta \rho_i}{\rho_i}\right| + \frac{\Delta t^*}{\nabla_i} \sum_{nb} A_{nb}\right] \Delta \tilde{W}_i = \frac{\Delta t^*}{\nabla_i} \sum_{nb} A_{nb} \Delta \tilde{W}_{nb} + \Delta \tilde{W}_i^*$$

where the subscript nb stands for a run over adjoining nodes $(i+1)$, $(i-1)$, $(j+1)$, and $(j-1)$. The parameter $\Delta t^* = \xi \Delta t_i$ with $\xi = 1.5$, a governing factor for the implicitness stability; $\Delta \tilde{W}_i^{**} = (\Delta u, \Delta v, \Delta T)^T$ quantify primitive explicit residuals (changes) of dependent variables as represented by Eqs. (19) and (21). The apparent benefit of $|\Delta \rho/\rho|$ included on the LHS of Eq. (22) is to enhance influence coefficients' diagonal-dominance; however, the term $|\Delta \rho/\rho|$ vanishes as the solution converges. Influence coefficients A_{nb} contains mass and diffusion fluxes. It is worth mentioning that the linearization of a positive source term associated with flow equations is no longer uncomplicated. Nevertheless, using a pseudo-linearization, the stiffness caused by the source term can be lowered [7].

The updating of primitive variables $\tilde{W} = (u^*, v^*, T)^T$ is subsequently prosecuted with the relation:

$$\tilde{W}^{n+1} = \tilde{W}^n + (\Delta u, \Delta v, \Delta T)^T \quad (23)$$

where recent values at the time level $(n+1)\Delta t$ are represented by \tilde{W}^{n+1} . With an arbitrary pressure field, Eq. (23) yields tentative velocity fields. Afterward, the tentative density ρ^* and sound speed C (may be designated as C^*) are estimated from Eq. (5) in conjunction with Eq. (10).

3.3. SIMPLE-corrector step

With the SIMPLE algorithm, continuity and momentum equations are not habitually convinced by computed variables. Consequently, repeated corrections to density, velocity and pressure fields are executed until the continuity constraint is satisfied. The u -velocity component is considered exclusively for convenience; velocity, pressure and density fields are corrected according to:

$$u = u^* + u' = u^* - \frac{\Delta t'}{\rho^*} \frac{\partial p'}{\partial x}, \quad p = p^* + p' \quad (24)$$

$$\rho = \rho^* + \rho' = \rho^* + \alpha_\rho p'/C^2, \quad \alpha_\rho = \begin{cases} 1 & \text{if } M_l \geq 0.3 \\ 0 & \text{otherwise} \end{cases}$$

where ρ' , u' and p' are the respective incremental density, velocity and pressure fields. In the current research, the associated weighting factor $\Delta t'_i$ with the pressure-velocity correction equation is determined using the spatially varying pseudo-time step Δt_i [6] and Eq. (22) as:

$$\Delta t'_i = \max \left(\Delta t_i, \frac{\nabla_i}{A_i} \right) \quad A_i = \sum_{nb} A_{nb} \quad (25)$$

in order to adapt better scaling and controlling, pertaining to both velocity and pressure corrections. To enhance stability and convergence in SIMPLE-like algorithms, the choice of $\Delta t'$ is an excellent alternative. Coefficients A_i are obviously achievable from discretized

momentum equations, retaining diffusion and volumetric mass fluxes.

Noteworthy, a nearly incompressible or weakly compressible flow is obtained for $\rho = \rho_r$ (reference constant density) when $\alpha_\rho = 0$ in Eq. (24); alternatively, with $M_l < 0.3$ the density tends to be uncorrelated with local pressure variations and therefore, the flow experiences a negligible compressibility effect. However, the density remains inconstant in some situations; such an example is the natural convection flow wherein the density changes with a variation in temperature. An appropriate solution to this problem is to use the full compressible solver, allowing density variations with respect to temperature variations.

The incremental velocity u' can be associated with the incremental pressure p' on a non-orthogonal grid by [6]:

$$u_i = u_i^* - \frac{\Delta t'_i}{\rho} \frac{(S_{nx} \partial p')_i + (S_{nx} \partial p')_j}{\nabla_i} \quad (26)$$

with

$$\frac{(S_{nx} \partial p')_i}{\nabla_i} \approx \frac{(n_x p')_{i+1/2} - (n_x p')_{i-1/2}}{\Delta n_i} \quad (27)$$

$$\frac{(S_{nx} \partial p')_j}{\nabla_j} \approx \frac{(n_x p')_{j+1/2} - (n_x p')_{j-1/2}}{\Delta n_j} \quad (28)$$

where p' is calculated using an averaging between neighboring nodal points; respective cell thicknesses Δn_i and Δn_j are defined in the i and j directions.

In compressible flows, changes in the pressure field alter density and velocity fields. Therefore, density and velocity fields must be corrected with the SIMPLE method to motivate the mass conservation; consequently, linearizing the mass flux ρu yields:

$$(\rho^* + \rho')(u^* + u') = \rho' u' + \rho^* u' + \rho' u^* + \rho^* u^* \quad (29)$$

Noteworthy, the emerging product $(\rho' u')$ with a second-order identity in Eq. (29) imports a tiny correction term compared to other products. It has an insignificant impact on the final solution field or convergence rate and therefore, it is usually neglected. A PCE can be constructed from the modified mass continuity equation accompanied by relations (25) and (26); using Eqs. (5)–(10) and the chain rule provide:

$$\frac{\partial p'}{\partial t} + \vec{u}^* \cdot \nabla p' - \Delta t' C^2 \nabla^2 p' = -C^2 \left(\frac{\partial \rho^*}{\partial t} + \nabla \cdot (\rho^* \vec{u}^*) \right) \quad (30)$$

Eq. (30) represents a convection-diffusion equation with source terms entitled as the mass imbalance and time-derivative of density; they constitute the driving force for the PCE. The total density variation can be split into two segments as follows:

$$\rho^{n+1} - \rho^n = (\rho^{n+1} - \rho^*) + (\rho^* - \rho^n) \quad (31)$$

where the first segment on the RHS of Eq. (31) is modeled as

$$\rho^{n+1} = \rho^* + \rho' = \rho^* + p'/C^2$$

which is given by (24) and the time derivative of $(\rho^* - \rho^n)$, i.e., $\partial \rho^*/\partial t$ (of course, naturally stems from the derivation) is included on the RHS of Eq. (30). As mentioned earlier, both ρ^* and C are calculated in the SIMPLE predictor-step; ρ^n is the estimated density from preceding cycle. The term $(\rho^* - \rho^n) = \Delta \rho^*$ can be recast using an EOS as:

$$\Delta \rho^* = \frac{\partial \rho}{\partial p} p' + \frac{\partial \rho}{\partial h} \Delta h = \frac{\partial \rho}{\partial p} p' + \frac{\partial \rho}{\partial T} \Delta T, \quad \frac{\partial \rho}{\partial T} = -\frac{p}{RT^2} = -\frac{\rho}{T} \quad (32)$$

Intuitively, Eq. (32) can be interpreted such that $\Delta \rho^*$ receives implicit contributions from the advection of p' [for instance, $\partial p'/\partial t + \vec{u}^* \cdot \nabla p' = 0$ in Eq. (30) and $p' = p^{n'} - (\vec{u}^{n'} \cdot \nabla p^n) \Delta t$ using a forward Euler time step; therefore, restrictions must be relaxed on

this pseudo-transport term $\partial p'/\partial t + \vec{u}^* \cdot \nabla p'$, i.e., the contribution of pressure-correction advection to the total mass source in Eq. (30) can naturally be ignored] and the change in specific enthalpy h or temperature T ; $\Delta \rho^*$ disappears at an incompressible flow since $\rho^* \approx \rho^n$. The neglect of $\partial \rho^*/\partial t$ in a compressible flow invokes another flaw to introducing UR factors with pressure-velocity corrections [4].

A truncated PCE is obtained when relations like Eqs. (18) and (26) are applied to the finite-volume discretization of Eq. (30):

$$\left[1 + \frac{\Delta t^*}{\nabla_i} \left(\sum_{nb} B_{nb} + \dot{m}_i^* \right) \right] p_i' = \frac{\Delta t^*}{\nabla_i} \sum_{nb} B_{nb} p_{nb}' - c_i^2 \left(\Delta \rho_i^* + \frac{\Delta t_i}{\nabla_i} \dot{M}_i^* \right) \quad (33)$$

Since volumetric flows in and out are not always equal for a compressible flow, the volumetric mass flux \dot{m}_i^* is included on the LHS of Eq. (33) due to the first-order upwind differencing that guarantees the diagonal dominance in influence coefficients. Symbolic parameters are represented as follows:

$$\begin{aligned} \text{sum}_{nb} B_{nb} &= B_{i+1/2} + B_{i-1/2}, \quad \dot{m}_i^* = (U^* S)_{i+1/2} - (U^* S)_{i-1/2} + (V^* S)_{j+1/2} - (V^* S)_{j-1/2} \\ B_{i-1/2} &= \left(\frac{c^2 \Delta t^* S}{\Delta n} + \max[U^* S, 0] \right)_{i-1/2}, \quad B_{i+1/2} = \left(\frac{c^2 \Delta t^* S}{\Delta n} + \max[-U^* S, 0] \right)_{i+1/2} \\ B_{j-1/2} &= \left(\frac{c^2 \Delta t^* S}{\Delta n} + \max[V^* S, 0] \right)_{j-1/2}, \quad B_{j+1/2} = \left(\frac{c^2 \Delta t^* S}{\Delta n} + \max[-V^* S, 0] \right)_{j+1/2} \end{aligned}$$

Eq. (33) retains the fictitious mass imbalance \dot{M}_i^* which can be defined by:

$$\begin{aligned} \dot{M}_i^* &= \dot{M}_{i+1/2}^* - \dot{M}_{i-1/2}^* + \dot{M}_{j+1/2}^* - \dot{M}_{j-1/2}^* \\ \dot{M}_{i\pm 1/2}^* &= (\rho^* U^* S)_{i\pm 1/2}, \quad \dot{M}_{j\pm 1/2}^* = (\rho^* V^* S)_{j\pm 1/2} \end{aligned} \quad (34)$$

To this end, it can be emphasized that using a thin-layer approximation, cross-diffusion fluxes in Eq. (33) are neglected with a view to maintaining diagonally dominant coefficient matrices [6,22]. Moreover, the tentative cell-face mass flux when calculated using a Newton-type linearization becomes superior to the fixed-point approach since this artifact induces a smooth transition of the characteristic PCE from the elliptic to hyperbolic one, respectively from the subsonic to supersonic flow regime [8]. Therefore, the tentative mass flux is computed on the cell-face $(i + 1/2)$ as:

$$(\rho^* U^*)_{i+1/2} = \hat{\rho}^* \bar{U}^* + \bar{p}^* \tilde{U}^* - \bar{p}^* \bar{U}^* \quad (35)$$

where a Newton-type linearization is employed and the meaning of 'overbar' is mentioned previously. The tentative velocity \bar{U}^* at the cell-face applies the reconstructed dissipation approach in Eq. (18) and the cell-face tentative density $\hat{\rho}^*$ is computed with the MUSCL scheme using a minmod limiter [23]. Articulately, $\hat{\rho}^* \bar{U}^*$ prevails over $\bar{p}^* \tilde{U}^*$ with hypersonic regimes, whereas characteristics are reversed with low-Mach number flows. Since the temperature field is estimated in the SIMPLE-predictor step, the local sound speed, total enthalpy and internal energy are renovated utilizing updated density, pressure and velocity fields:

$$C = \sqrt{\gamma p / \rho}, \quad H = c_p T + u^2/2, \quad E = H - p/\rho \quad (36)$$

Using an EOS, other thermodynamic parameters can also be updated at this juncture. Physically, Eq. (33) has a close resemblance to the algebraic Eq. (22). Undoubtedly, the proposed algorithm is capable of working at all speeds having a symmetric pressure-gradient stencil without switching additional compressibility terms off when simulating incompressible flows. Obviously, the numerical coding for a 3-D case with the current solver is quite straightforward and simple.

4. Algorithmic solution sequences

Reference [7] provides a detailed description of the boundary conditions. Discretized equations are solved using a tridiagonal matrix algorithm (TDMA). Solution Sequences involved in the 2-D solver are handed out as shown in Fig. 1. All flow-field variables are initialized at the beginning of iteration cycle. Afterward, momentum and energy equations are solved to attain tentative fields using Eqs. (19)–(23), given that Eq. (17) is used to evaluate pressure-gradients in momentum equations. Next the tentative density ρ^* and sound speed C are calculated from Eq. (5) in conjunction with Eq. (10). The cell-face mass flux $(\rho^* U^*)_{i\pm 1/2}$ is determined from relations like Eq. (35) in forming the mass-imbalance \dot{M}_i^* , accompanied by $\Delta \rho^*$. The pressure-correction Eq. (33) is then solved for p' . Finally, density, velocity, pressure and energy fields are updated using Eqs. (24) and (36). The sound speed and other thermodynamic variables are also renewed. The algorithmic design shown by the flowchart in Fig. 1 could also be described in pseudo-flow diagram as demonstrated in Fig. 2.

5. Flow with low-Mach number

Note that 'incompressible' means constant property simulations and 'compressible' signifies variable property simulations with low-Mach number flows. To speed up reliability and generality with a single model solving a compressible or incompressible flow, the computational experiment concentrates on a buoyancy-driven flow in a square cavity. This test-case preserves a strong source term which obviously reinforces the states of enhanced effectiveness and robustness, justifying the predictive performance of a numerical solver. The accuracy of computations obtained from the proposed algorithm is validated against benchmark-quality literature data [24–26] and results of CVFEM (control-volume based finite-element method) with vorticity stream function formulation [27]. Compressible flows usually deal with large pressure gradients which induce density variations due to the compression; however, the buoyancy-driven flow exhibits large variations in density due to a high energy deposition. An FUS scheme with no limiter function is applied to calculated state variables $(p, u, v, H)_L$ and $(p, u, v, H)_R$ associated with inviscid fluxes and Eqs. 17,18.

Grid-independent numerical solutions have been confirmed by recommended computational grids in the current research. Applied grid resolutions approve computational errors less than 2% for all dependent variables relying on grid-dependence tests. The following relations are used to calculate local and average Nusselt numbers:

$$Nu = -\frac{\partial \theta}{\partial x} \Big|_{x=0}, \quad Nu_{av} = \frac{1}{L} \int_0^L Nu dx \quad (37)$$

where $\partial \theta / \partial x$ is approximated using a three-point one-sided finite-difference formula; the dimensionless x -coordinate, characteristic length and temperature are respectively indicated by x, L and θ .

Reference [7] represents a diagrammatic 2-D buoyancy-driven cavity filled with a perfect gas. A dimensional characteristic length of \hat{L} with horizontal adiabatic top and bottom walls is assigned to the physical model. Isothermal temperatures with \hat{T}_c and \hat{T}_h , respectively are imposed on vertical cold and hot walls. The 2-D configuration uses dimensionless governing equations. Reference scales are applied to non-dimensionalize all dimensional parameters; a 'hat-sign' is used to designate dimensional variables, given in Reference [28] where quantities $\hat{g}, \hat{\nu}_r = \hat{\mu}_r / \hat{\rho}_r$ and $\hat{\alpha}_r$ are respectively the gravitational acceleration, kinematic viscosity and thermal diffusivity. Dimensionless specific heats c_v and c_p , reference pressure, specific enthalpy h and internal energy e can be obtained

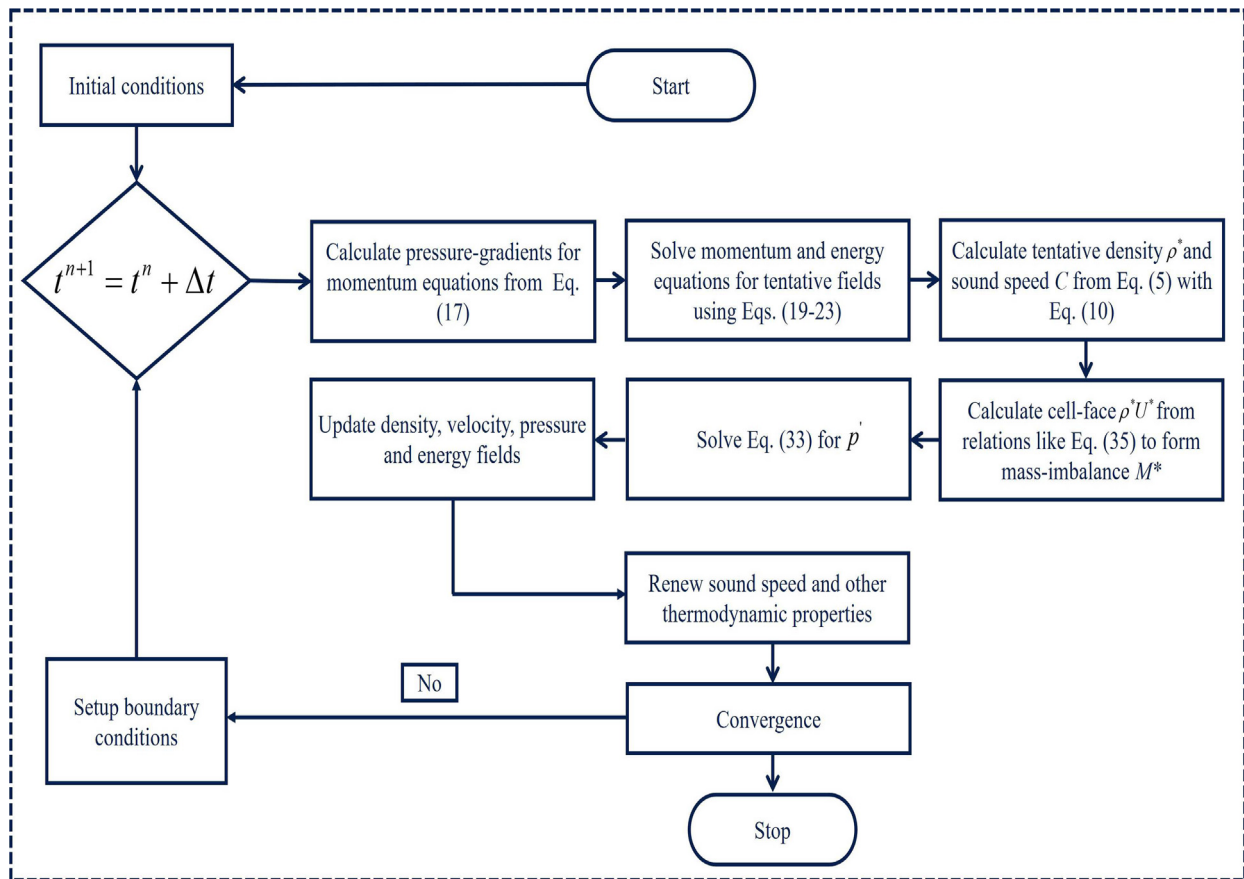


Fig. 1. Flowchart for all-speed flow SIMPLE algorithm.

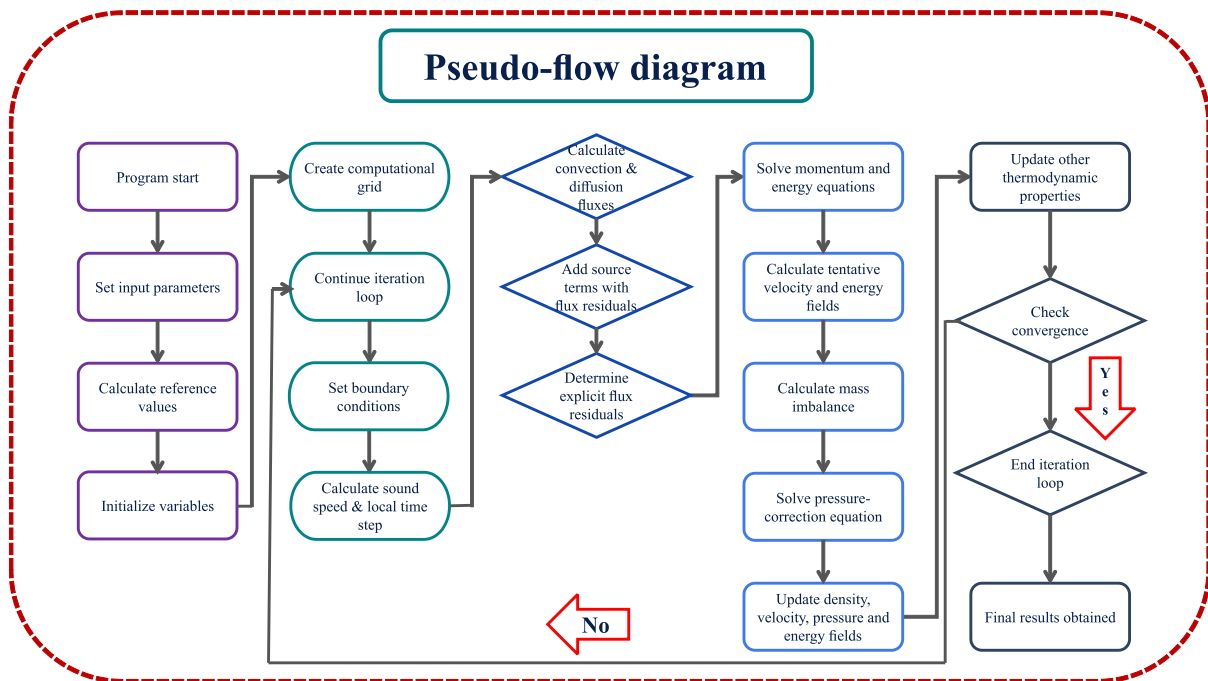


Fig. 2. Pseudo-flow diagram for all-speed flow SIMPLE algorithm.

from $c_p = \gamma R / (\gamma - 1)$, $\gamma = c_p / c_v$ and $p = \rho RT$. Sutherland's law is used to evaluate the dynamic viscosity: $\hat{\mu}_r = \hat{\mu}^* (\hat{T}_r / \hat{T}^*)^{3/2} (\hat{T}^* + \hat{S}^*) / (\hat{T}_r + \hat{S}^*)$ with $\hat{T}^* = 273K$, $\hat{S}^* = 110.5K$ and $\hat{\mu}^* = 1.68 \times 10^{-5} kgm^{-1}s^{-1}$. Two dominated non-dimensional parameters for the test-case spring from the normalization: Prandtl number Pr and Grashoff number, $Gr = 2g\epsilon$ with the dimensionless temperature difference $\epsilon = (\hat{T}_h - \hat{T}_c) / (2\hat{T}_r)$ where $\hat{T}_r = (\hat{T}_h - \hat{T}_c) / 2$. To validate numerical simulations against other benchmark data [24–26] and CVFEM [27] solutions, present computations set $Pr \approx 1.0$. A dimensionless reference velocity is defined as $U_r = \sqrt{Gr}$ [7]. Another dimensionless dominant parameter for the buoyancy-driven flow in a square cavity is the Rayleigh number Ra given by $Ra = GrPr$; nonetheless, $Ra = Gr$ since $Pr = 1.0$. Chosen reference values are: $\hat{\rho}_r = 0.5884 kg/m^3$, $\hat{g} = 9.81 m/s^2$, $\hat{T}_r = 600K$ and $\hat{L} = 1m$; other technical details are given in Reference [15] for this test-case.

No-slip boundary conditions are prescribed at all solid walls; bottom and top horizontal walls utilize an adiabatic boundary condition. Corresponding to the above-mentioned perfect gas (air) model, transport properties in a compressible flow vary with temperature while Pr remains constant. The Sutherland formula is used to evaluate the viscosity μ and the definition of Pr determines thermal conductivity λ :

$$\mu = \frac{1 + \hat{S}^*/\hat{T}_r}{T + \hat{S}^*/\hat{T}_r} T^{3/2}, \quad \lambda = \frac{\mu c_p}{Pr} \quad (38)$$

The temperatures of hot and cold vertical walls are respectively $T_h = 1 + \epsilon$ and $T_c = 1 - \epsilon$ with $0 < \epsilon < 1$. Compressible equations retain the following source terms:

$$f = \begin{pmatrix} 0 \\ 0 \\ -\rho g \\ -\rho g v \end{pmatrix} = \begin{pmatrix} 0 \\ 0 \\ -(\rho - 1)g \\ -(\rho - 1)g v \end{pmatrix} \quad (39)$$

where the relation $g = Gr / (2\epsilon)$ is used to calculate non-dimensional values for g . Remarkably, both source term formulations in Eq. (39) have identical effects. However, it is convenient to work with $f = [0, 0, -(\rho - 1)g, -(\rho - 1)g v]^T$ for low Mach number flows. Phenomenal transport equations with this transformation are physically much more understandable since they have a close resemblance to Boussinesq equations and the numerical method is benefited with a rapid convergence. As a matter of fact, this test-case preserves strong advective near-wall and diffusive central regimes, representing a relevant numerical problem to justify the efficacy of a newly developed solution algorithm. Results are presented in a form of v and $\theta = (T - T_c) / (T_h - T_c)$ versus x .

A nonuniform grid 40×40 for $Gr = 10^5$, 50×50 for $Gr = 10^6$, 60×60 for $Gr = 10^7$ and 80×80 for $Gr = 10^8$ have been deployed with denser grid points at the wall-vicinity than those of the core for numerical simulations. Numerical computations with chosen nonuniform grid resolutions are adequate to speculate consistency and reliability, pertaining to the present formulation. Current investigations are further supported by available literature and computational data [24–27]. Initial guesses are: $u = v = 0.1U_r$, pressure-difference $\Delta p = 0$ and $T = (T_h + T_c) / 3$; the selected problem encloses the reference Mach number M_r in a span of $10^{-5} < M_r < 10^{-2}$.

To build an equivalency between incompressible and compressible models within the incompressible limit, the test-case is designed for $\epsilon = 0.01$ with a temperature difference $2\epsilon\hat{T}_r = \Delta\hat{T} = 12K$. Assuming constant properties with Boussinesq

approximation, full-compressible equations are therefore solved for incompressible flow with source terms $f = (0, 0, GrT, GrTv)^T$. Isothermal boundary conditions are imposed; they are $T_h = 1.0$ on the hot and $T_c = 0$ on the cold vertical walls. Shown in Fig. 3 are the distributions of vertical velocity, temperature and local Nusselt number Nu at $Gr = 10^5$; $\epsilon = 0.01$ refers to the incompressible solution and other values for ϵ with $\Delta\hat{T} = (240K, 480K, 720K)^T$ indicate compressible simulations. CVFEM computations from dimensionless incompressible Navier-Stokes (NS) equations with a decoupled simplified energy equation [20] are included for comparison. As can be seen, incompressible computations have an excellent agreement with CVFEM data. Qualitatively, temperature solutions from both incompressible and compressible formulations seem to be almost identical; this is to be anticipated since both model thermal-diffusion terms are apparently similar. Nevertheless, large density variations with increasing $\Delta\hat{T}$ induce noticeably different velocity profiles with both methods. Consequently, the boundary-layer thicknesses of velocity and temperature become distinguishably dissimilar, indulging in different wall heat fluxes.

Fig. 3 highlights obviously on the Boussinesq approximated validity domain (e.g., approximately $\Delta\hat{T} < 28K$ [29]); temperature differences $\Delta\hat{T} = (240K, 480K, 720K)^T$ cross the limit of Boussinesq approximation. Compared to incompressible solutions, non-symmetric temperature and vertical velocity profiles are observed on the horizontal midplane; the nonisotropic character of density, generated from large temperature variations gives rise to this phenomenon. In other words, compressible solution asymmetries result from the gas-expansion with a decrease in density near the hot-wall region and the gas-contraction with increasing density near the cold-wall region. Apparently, the boundary layers of velocity and temperature in the cold-wall regions are narrower than those of the hot-wall regions. In addition, the absolute magnitude of vertical velocity in the hot wall-vicinity is higher than that of in the cold-wall region. Since a change in density with changing temperature is reimbursed by reconcilable changes in velocities, present simulations naturally satisfy the mass conservation. As mentioned earlier, g is determined from $g = Gr / (2\epsilon)$; with decreasing non-dimensional temperature difference ϵ , the magnitude of g increases. However, variations in density and velocity respond according to the mass flux $\rho\vec{u}$ to satisfy the mass continuity constraint; the density at $\epsilon = 0.2$ is higher than that of at $\epsilon > 0.2$ and therefore, the convective velocity at $\epsilon = 0.2$ is lower than that of at $\epsilon > 0.2$, leading to an increase in the Nu -distribution with $\epsilon = 0.2$ at the wall-proximity (e.g., lower part of heated wall) in Fig. 3, confirming that these characteristics are compatible with those of literature data [29].

A further extension to the present study is accomplished with $\epsilon = 0.3$ (i.e., $\Delta\hat{T} = 360K$), implying that the flow confronts a significant compressibility effect and $\epsilon = 0.01$ indicates an incompressible setup with the Boussinesq approximation as mentioned earlier. Perhaps, a predominant precursor to the advancement of compatible designs associated with complex engineering applications could be initiated by a diversified scanning of heat and fluid flow in a fundamental configuration similar to the buoyancy-dominated natural convection in a square cavity. To be concise, flow computations at $Gr = 10^8$ (after which laminar-to-turbulence transition may occur) are considered.

Figs. 4(a) and 4(b) displays respective profiles of vertical velocity and temperature on the horizontal midplane at $Gr = 10^8$. Included are the incompressible CVFEM computational data for comparisons. It seems likely that an encouraging qualitative agreement is obtained when present incompressible simulations are compared with CVFEM data. Nevertheless, the symmetry of velocity and temperature distributions is affected due to compressible-

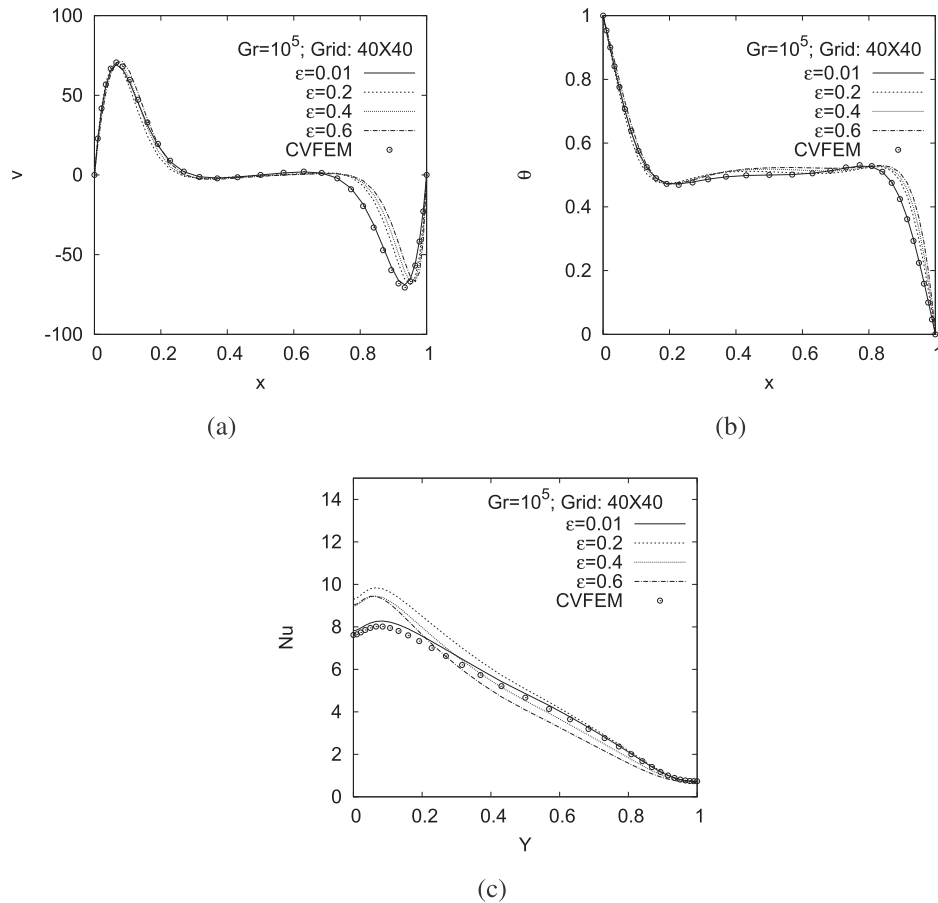


Fig. 3. Profiles of buoyancy-driven cavity flow: (a) horizontal-midplane velocity; (b) horizontal-midplane temperature and (c) Nu across heated wall.

flow simulations with variable thermodynamic properties. This occurrence has been launched because of the mass conservation, facing large density changes due to large temperature differences. This feature is compatible with the physical anticipation.

Fig. 4(c) exhibits local Nusselt number profiles along the hot vertical wall for the natural convection flow. CVFEM results are also plotted in the same figure for a comparison purpose. It is apparent that incompressible simulations match CVFEM data fairly well. Almost identical solutions are reproduced; however, due to methodological differences, incompressible computations show minor variations in Nusselt number profiles when compared with CVFEM data. Along much of the heated vertical wall height, Nu-distributions from compressible simulations reasonably match incompressible and CVFEM solutions. Nonetheless, the compressible model over-estimates the Nu-profile at the lower portion of hot vertical wall, a detailed discussion of which is provided earlier.

With same initial conditions, Fig. 4(d) manifests the mass-imbalance convergence history which is defined as the root-mean-square of fictitious mass residuals M^* against iteration counters. The algorithm employs no pseudo-linearization for positive source terms. Both incompressible and compressible models apply an equal CFL number (unoptimized) for numerical simulations to reflect on convergence behaviors. The performance trends with an equivalent CFL number speculate that incompressible simulations outperform compressible simulations. Interestingly, the compressible convergence plot runs parallel to that of incompressible one; this is due to the fact that the former method negotiates a mutual remuneration between velocity and density fields to convince the mass constraint. In contrast, a totally one-sided feature is associated with the incompressible scheme; the discrete conti-

nunity constraint is brought into conformity with the approximated velocity field. Conclusively, the optimization of Boussinesq approximated compressible algorithm benefits the incompressible model.

For the buoyancy-driven flow, a quantitative comparison made from magnitudes of Nu_{av} at the heated vertical wall and maximum vertical velocity V_{max} on the horizontal midsection is illustrates in Table 1. Presumably, enthusiastic researchers receive a profound encouragement from such a sensible tabular evaluation. As can be observed, results generated by compressible and incompressible models maintain a reasonable correspondence with benchmark data in the literature [24–26]. Since almost negligible differences can be ascertained from tabulated values, the overall compressible algorithmic architecture is eventually non-dissipative as advocated by the tabular investigation. Nevertheless, appreciable variations are distinguishable in velocity and temperature profiles adhering to incompressible and compressible flows.

Another variable property simulation is conducted for $\epsilon = 0.6$ where $T_h = 1 + \epsilon$ and $T_c = 1 - \epsilon$ indicate the hot and cold vertical-wall temperatures, respectively. For this setup $Pr = 0.71$ which is independent of temperature variations; however, the compressibility effect is rigorously dominant on the flow. The relation $g = Ra/(2\epsilon Pr)$ is used to evaluate non-dimensional values for g . A 60×60 grid for $Ra = 10^6$ and 80×80 for $Ra = 10^7$ with denser grid points at near-wall regimes than those of the core, have been arranged for simulations. Literature data [30,31] for $\epsilon = 0.6$ with $\Delta T = 720K$ further reinforces the present appraisals.

Table 2 contrasts Nu_{av} at the heated vertical wall obtained from the SIMPLE algorithm with those of available data [30,31]. For this buoyancy-driven compressible (variable property) cavity flow, References [30,31] admit that almost identical average Nusselt num-

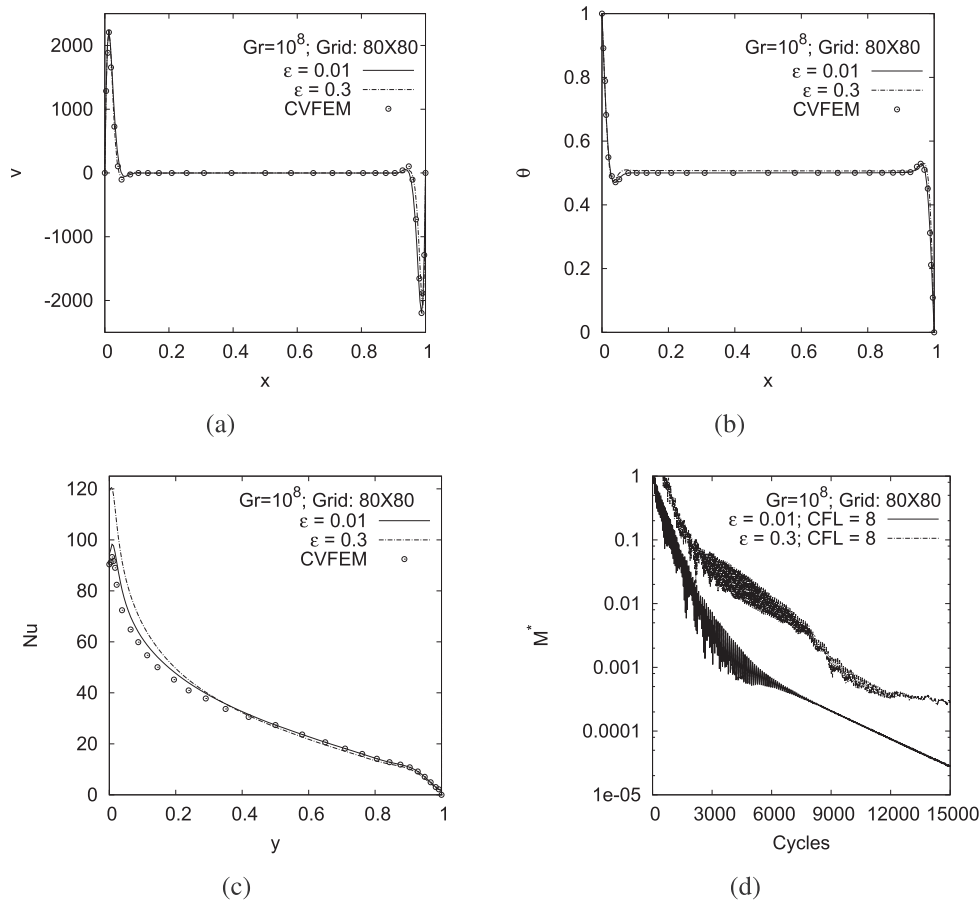


Fig. 4. Profiles of buoyancy-driven cavity flow: (a) horizontal-midplane velocity; (b) horizontal-midplane temperature; (c) Nu across heated wall and (d) mass-imbalance convergence.

Table 1

Natural convection in cavity: comparisons of Nu_{av} at hot-vertical wall and V_{max} at midsection $y = 0.5$ with reference data.

Parameter	Ref. [24]	Ref. [25]	Ref. [26]	$\epsilon = 0.01$	$\epsilon = 0.3$
$Gr = 10^5$					
V_{max}	70.81	68.66	70.33	69.5	71.0
Nu_{av}	4.60	4.57	4.63	4.80	5.0
$Gr = 10^6$					
V_{max}	228.05	222.70	226.6	221.90	224.10
Nu_{av}	8.98	9.02	9.11	9.45	9.80
$Gr = 10^7$					
V_{max}	720.54	706.30	706.91	687.50	697.80
Nu_{av}	16.66	16.80	17.03	17.74	18.70
$Gr = 10^8$					
V_{max}	2291.05	1935.0	2202.87	2206.0	2244.0
Nu_{av}	31.49	31.0	30.71	32.20	33.30

Table 2

Natural convection with variable properties (compressible identity): validation of Nu_{av} at hot vertical wall with reference data.

Parameter	Ref. [30]	Ref. [31]	SIMPLE
$Ra = 10^6$			
Nu_{av}	8.6824	8.6866	8.5820
$Ra = 10^7$			
Nu_{av}	16.1273	16.2410	16.0195

bers are conserved by both hot and cold vertical walls. As is observed, SIMPLE computations show a striking congruence with literature data. Discernibly, the current SIMPLE solver is conducive

to simulating industrial natural convection dominated flows subjected to huge temperature variations and thus, giving an opportunity to avoid the Boussinesq approximation.

6. Compressible numerical tests

The test Problems 1-D Sod shock-tube [16] and Mach 3 shock [17] are well-known as highly non-linear compressible flows; they are characterized by rarefactions, shocks and contact discontinuities. Conceptually clear and comprehensive results of these well-defined problems can be utilized to evaluate the performance of compressible SIMPLE solver. Conventionally, the chosen test-cases are solved using an explicit time-integration method accom-

panied by a specific upwind-type component. Air has been considered as the working fluid with $\gamma = 1.4$ and $c_p = 1005 \text{ J/kg}^{-1} \text{ K}^{-1}$; numerical test problems cover $M_l = |u|/C$ in a span of $0.9 \geq M_l \leq 3$. Computations have been conducted using a uniform 400×1 grid; 1-D Euler equations set $CFL \leq 0.2$ in accordance with a maximum magnitude of the convective velocity. An FUS scheme together with the minmod limiter is applied to evaluate non-viscous fluxes with 1-D Euler equations. Numerical simulations employ an explicit first-order backward Euler scheme (explicit predictor step) and an implicit corrector step within the SIMPLE framework to solve 1-D test problems. Therefore, the overall contrivance for considered 1-D test cases can be nominated as a semi-implicit scheme. The proposed compressible SIMPLE solver obtains an additional support for its efficacy from the computation of flow over an NACA-0012 airfoil. Current computations are compared with modified Roe and Lax-Wendroff [28] schemes; both models solve the Euler inviscid equations using a fully explicit first-order backward Euler method with conservative variables for 1-D test cases.

6.1. Shock-tube problem

The well-documented Sod's shock-tube [16] is selected to validate performances of the present compressible SIMPLE algorithm together with Roe and Lax-Wendroff methods. The shock-tube

retains a contact discontinuity, a shock wave and a rarefaction fan. The flow characteristics can be configured into the Riemann problem with discontinuous initial conditions as given in [16]. Either boundary can implement discontinuous initial boundary conditions for primitive variables. The solution to this test-case advances with $t = 0.01$ over the interval $x \in [0, 1]$ where x is the computational domain length.

Performances for all independent TVD schemes are demonstrated in Fig. 5. All three individual approaches replicate almost identical results as revealed by a careful investigation of shock-tube simulations. Conspicuously, the contact-discontinuity is resolved consistently, the shock is sensibly captured and a oscillation-free solution is obtained. All simulations match the exact solution well.

6.2. Mach 3 shock-tube

Competencies of three independent solvers are further assessed by computing a Mach 3 shock-tube problem [17]. The test-case reserves a sonic point, rich in a strong expansion fan. The evolution of flow field is initiated with discontinuous boundary conditions as given in [17]. Fig. 6 plots both numerical and analytic results; the figure reads out that corresponding to the analytic solution, all numerical approaches obtain a well-resolved expansion wave. In this setup, numerical simulations readily distinguish the right

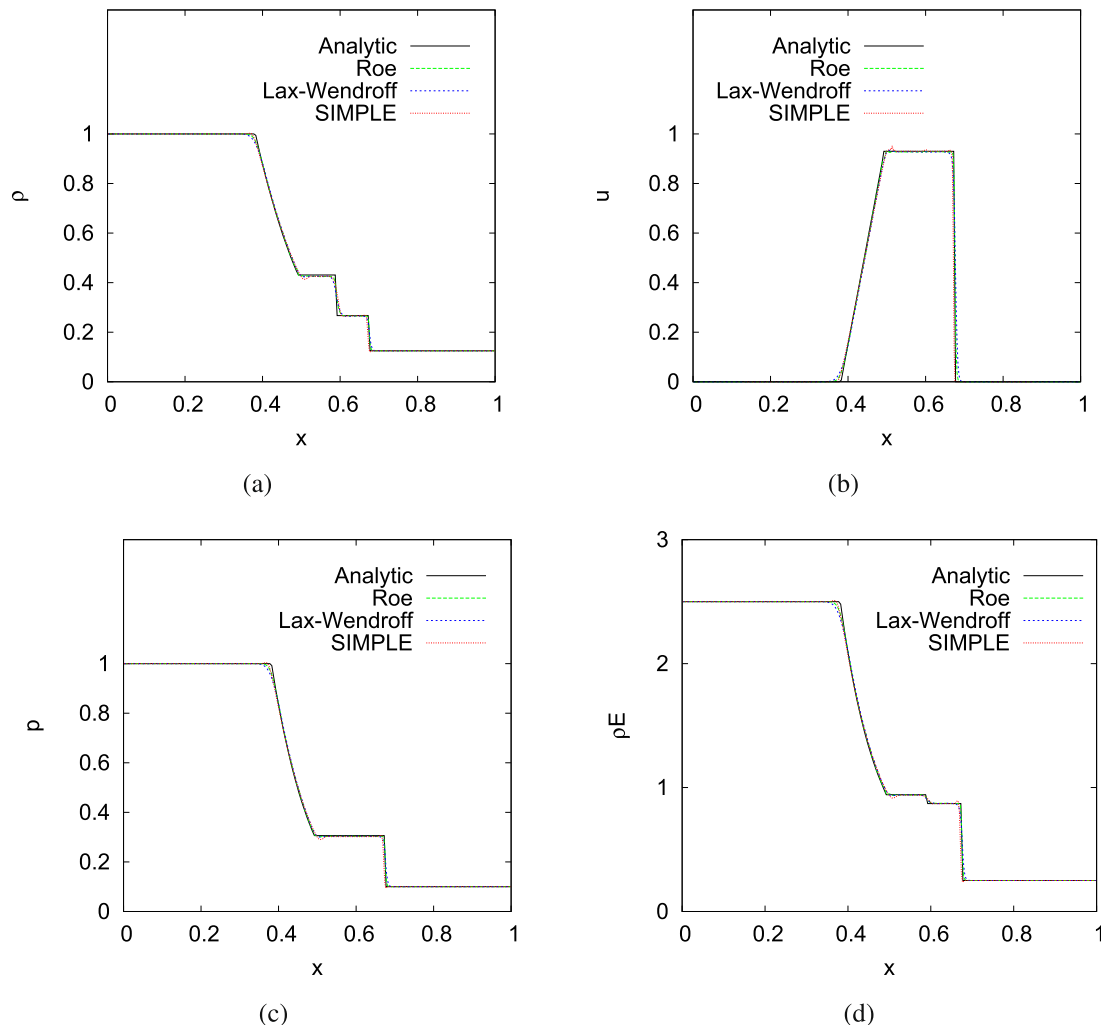


Fig. 5. Solutions of Sod's shock-tube after 0.1 second with various schemes: (a) density; (b) velocity; (c) pressure and (d) total internal energy.

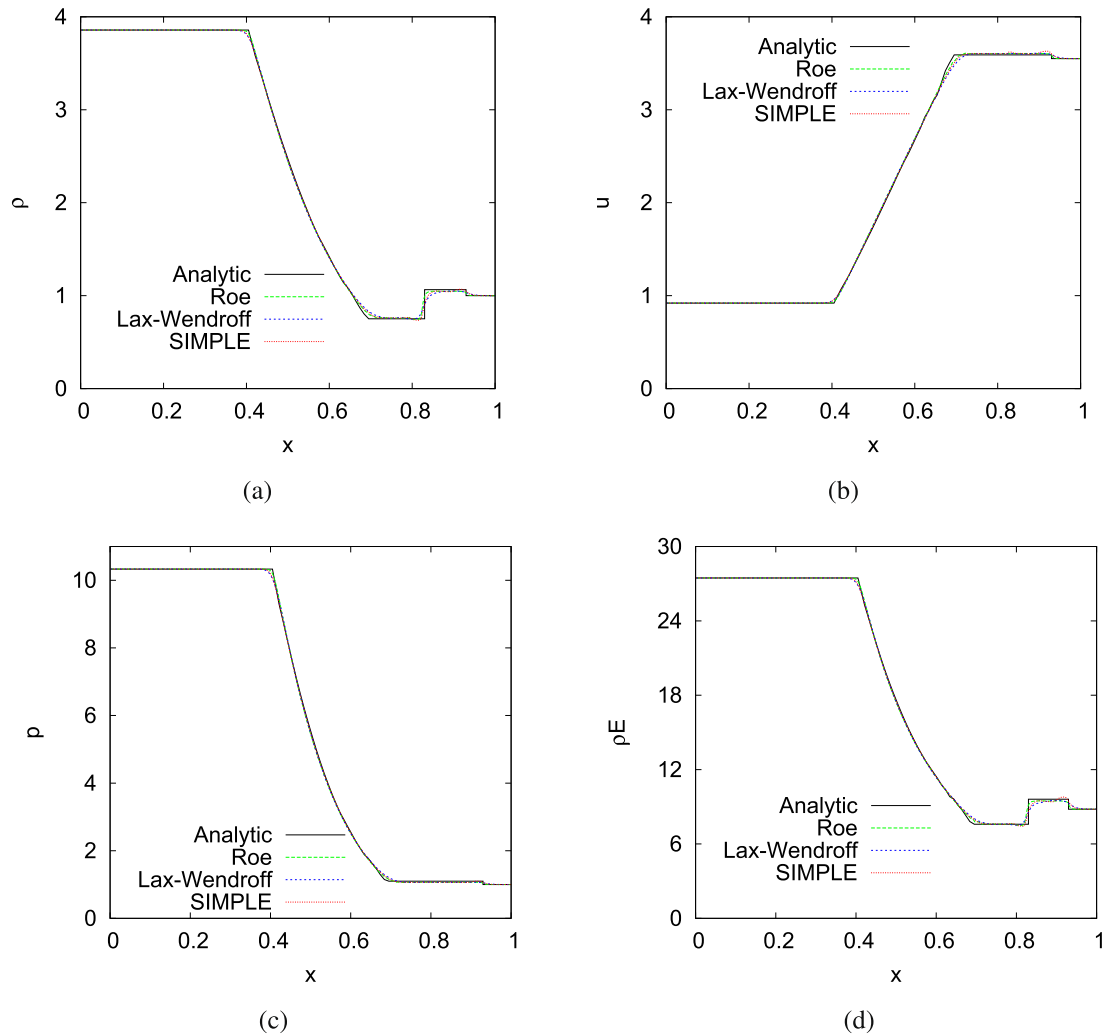


Fig. 6. Solutions of Mach 3 shock-tube after 0.09 second for different approaches: (a) density; (b) velocity; (c) pressure and (d) total internal energy.

moving-shock recognized by a tiny jump. A good congruence exists among all three independent numerical schemes.

6.3. Flow past an NACA-0012 airfoil

The flow over a familiar 2-D NACA-0012 airfoil is computed to further evaluate the competency of SIMPLE method. The reference Mach number $M_r = 0.5$ with a zero angle of attack. The Reynolds number $Re = 5000$ based on the chord length c ; this is a critical Re for this test-case since laminar-to-turbulence transition may occur after $Re > 5000$ [32]. A O-type nonuniform structured grid 126×92 has been deployed for numerical simulations with compressed grid points at near-wall regions. Fig. 7(a) displays the representative structured grid. Not shown, the computational experiment approves that this grid arrangement is sufficient to produce grid-independent numerical results. Far-field boundary conditions are prescribed at $15c$ away from the airfoil surface.

Chosen reference values are: $\hat{\rho}_r = 1.18 \text{ kg/m}^3$, $\hat{\mu}_r = 18.46 \times 10^{-6} \text{ N-s/m}^2$, $\hat{T}_r = 300 \text{ K}$ and $Pr = 0.71$. Similar to the buoyancy-driven cavity flow case, reference scales are used to non-dimensionalize all variables. The main dimensionless group evolving is $Re = \hat{\rho}_r \hat{u}_r c / \hat{\mu}_r$ and the reference velocity \hat{u}_r can be determined from a given Re . As mentioned earlier, a 'hat-sign' is used to indicate dimensional quantities. Dimensionless thermodynamic parameters can be calculated from an appropriate EOS. The

solid wall applies no-slip boundary conditions and $U_r = 1.0$. The temperature field imposes an adiabatic boundary condition on the airfoil surface. The specific heats of gas (air), dynamic viscosity and thermal conductivity are presumed to be not dependent on temperature; the dimensionless dynamic viscosity and thermal conductivity can be evaluated as:

$$\mu = \frac{1}{Re}, \quad \lambda = \frac{\mu c_p}{Pr} = \frac{\mu}{Pr(\gamma - 1)M_r^2} \quad (40)$$

Three independent flux-difference schemes work in collaboration with the SIMPLE algorithm and an FUS scheme is applied to evaluate inviscid fluxes. No limiter is used for Rusanov and Roe schemes; nonetheless, the Lax-Wendroff approach retains a TVD limiter from its derivation and the minmod slope limiter is used in this case. An appropriate EOS can be used to calculate the density ρ .

Fig. 7(b) shows the surface pressure coefficient C_p around the airfoil; a dimensionless chord length x/c is used in the plot. It appears that all three independent methods produce identical C_p solutions; as can be seen, simulations are compatible with literature data [32]. Fig. 7(c) displays mass-residual convergence histories for different flux-difference schemes. A $CFL = 5$ is chosen to highlight on the convergence behaviors for various flux-difference schemes. Evidently, Rusanov and Lax-Wendroff approaches exhibit an identical convergence. It seems likely that the Roe scheme behaves slightly different owing to its complex

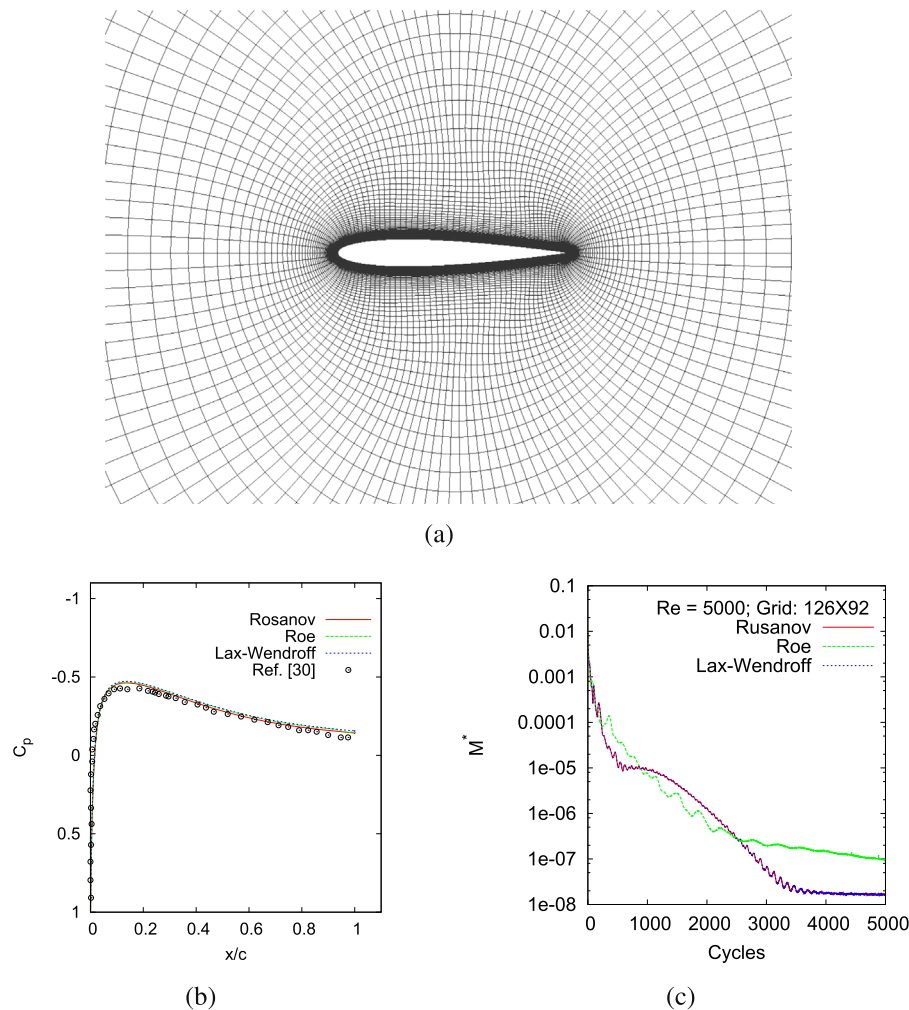


Fig. 7. NACA-0012 airfoil: (a) structured computational grid; (b) pressure coefficient and (c) mass-imbalance convergence.

dissipation scalings. Unambiguously, all schemes ascertain that the devised compressible SIMPLE algorithm suppresses non-physical oscillations during the iterative convergence.

7. Concluding remarks

To predict flows at all speeds, the SIMPLE algorithm is contrived on a collocated grid using a cell-centered finite-volume Δ -formulation. Influence coefficients' diagonal-dominance with the PCE is ensured. The fictitious mass imbalance is evaluated using an improved cell-face dissipation scheme together with a Newton-type linearization, enhancing the solver stability. The inclusion of $\partial p / \partial t \approx p' / \Delta t$ with the energy equation convokes a coupling between total enthalpy and pressure-correction, promoting the convergence acceleration. The Rusanov flux-difference scheme is modified to calculate inviscid fluxes at all Mach numbers. An indicator α_p based on the local Mach number imposes a constraint on the appropriate state of compressibility related to the updating of density in the corrector step. The SIMPLE algorithm with reformulated cell-face flux-difference and dissipation schemes is capable of eliminating non-physical numerical oscillations as dictated by convergence studies; the overall artifact strengthens the numerical stability of iterative solver. Results demonstrate that the incompressible simulation is benefited from augmented convergence and robustness when constant-property solutions optimize the compressible model. The current formula-

tion compares fairly with literature data and analytic solutions. The algorithm is expected to have stability at all-Mach number flows with an avoidance of UR factors.

Declaration of Competing Interest

The authors declare that they have no known competing financial interests or personal relationships that could have appeared to influence the work reported in this paper.

Acknowledgments

We are grateful to Hangzhou Dianzi University research and laboratory establishment supporting funds (Grant Nos. GK208800299001-006 & GK208803299001-013) of Zhejiang Province, P.R. China.

References

- [1] Karki KC, Patankar SV. Pressure based calculation procedure for viscous flows at all speeds in arbitrary configurations. *AIAA J* 1989;27(9):1241–9.
- [2] Moukalled F, Darwish M. A unified formulation of the segregated class of algorithms for fluid flow at all speeds. *Numer Heat Transf Part B* 2000;37:103–39.
- [3] Demird'zić I, Lilek V, Perić M. A collocated finite volume method for predicting flows at all speeds. *Int J Numer Meth Fluids* 1993;16:1029–50.
- [4] Miettinen A, Siikonen T. Application of pressure- and density-based methods for different flow speeds. *Int J Numer Meth Fluids* 2015;79:243–67.

- [5] Patankar SV. Numerical Heat Transfer and Fluid Flow, Hemisphere, Washington, DC; 1980.
- [6] Rahman MM, Siikonen T. An Improved SIMPLE Method on a Collocated Grid. *Numer Heat Transf Part B* 2000;38:177–201.
- [7] Rahman MM. Avoiding under-relaxations in SIMPLE algorithm. *Numer Heat Transf Part B* 2020;52(5). doi: <https://doi.org/10.1080/10407790.2020.1787043>.
- [8] Denner F. Fully-coupled pressure-based algorithm for compressible flows: linearisation and iterative solution strategies. *Comput Fluids* 2018;175:53–65.
- [9] Rhie CM, Chow WL. Numerical study of the turbulent flow past an airfoil with trailing edge separation. *AIAA J* 1983;21:1525–32.
- [10] Rahman MM, Miettinen A, Siikonen T. Modified SIMPLE formulation on a collocated grid with an assessment of the simplified Quick scheme. *Numer Heat Transf Part B* 1996;30:291–314.
- [11] Rahman MM, Siikonen T. A dual-dissipation scheme for pressure-velocity coupling. *Numer Heat Transf Part B* 2002;42:231–42.
- [12] Ong KC, Chan A. 2016, A pressure-based Mach-uniform method for viscous fluid flows. *Int J Comput Fluid Dyn* 2016;30(7–10):516–30. doi: <https://doi.org/10.1080/10618562.2016.1245417>.
- [13] Hussin MS, Ghorab A, El-Samanoudy MA. Computational analysis of two-dimensional wing aeroelastic flutter using Navier-Stokes model. *Ain Shams Eng J* 2018;9:3459–72.
- [14] Rusanov V-V. Calculation of the intersection of non-steady shock waves with obstacles. *iUSSR Comput Math Math Phys* 1962;1(2):304–20.
- [15] Vierendeels J, Merci B, Dick E. Benchmark solutions for the natural convective heat transfer problem in a square cavity with large horizontal temperature differences. *Int J Numer Meth Heat Fluid Flow* 2003;13(8):1057–78.
- [16] Sod GA. A survey of several finite difference methods for systems of nonlinear hyperbolic conservation laws. *J Comput Phys* 1978;27:1–31.
- [17] Arora M, Roe P.A well-behaved TVD limiter for high resolution calculations of unsteady flow. *J Comput Phys* 1997;132(1):3–11.
- [18] Rahman MM, Siikonen T. An artificial compressibility method for incompressible flows. *Numer Heat Transf Part B* 2001;40:391–409.
- [19] Rahman MM, Siikonen T. An artificial compressibility method for viscous incompressible and low Mach number flows. *Int J Numer Meth Eng* 2008;75:1320–40.
- [20] Roller S, Munz CD. A low Mach number scheme based on multi-scale asymptotics. *Comput Visualiz Sci* 2000;3:85–91.
- [21] Anderson WK, Thomas JL, Van Leer B. Comparison of finite volume flux vector splittings for the Euler equations. *AIAA J* 1983;24:649–64.
- [22] Rahman MM, Siikonen T, Miettinen AA. Pressure correction method for solving fluid flow problems on a collocated grid. *Numer Heat Transf Part B* 1997;32:63–84.
- [23] Roe PL. Some contributions to the modeling of discontinuous flows. *Lect Notes Appl Math* 1985;22:162–93.
- [24] Wan DC, Patnaik BSV, Wei GW. A new benchmark quality solution for the buoyancy driven cavity by discrete singular convolution. *Numer Heat Transf Part B* 2001;40:199–228.
- [25] Malan AG, Lewis RW, Nithiarasu P. An improved unsteady, unstructured, artificial compressibility, finite volume method for viscous incompressible flows: part II. Application. *Int J Numer Meth Eng* 2002;54:715–29.
- [26] Massarrotti N, Arpino F, Lewis RW, Nithiarasu P. Explicit and Semi-implicit CBS Procedures for Incompressible Viscous Flows. *Int J Numer Meth Eng* 2006;66:1618–40.
- [27] Rahman MM, Lampinen MJ. Numerical study of natural convection from a vertical surface due to combined buoyancies. *Numer Heat Transf Part A* 1995;28:409–29.
- [28] Rahman MM. Compromising with corrector step of SIMPLE algorithm. *Math Comput Simul* 2021;188:135–63.
- [29] El-Gendi MM, Aly AM. Numerical simulation of natural convection using unsteady compressible Navier-stokes equations. *Int J Numer Meth Heat Fluid Flow* 2017;27(11):2508–27.
- [30] Ouazzani J, Garrabos Y. A novel numerical approach for low Mach number: application to supercritical fluids. In: *Proceedings of ASME 2013 Summer Heat Transfer Conference HT2013-17732*.
- [31] Le Quere P, Weisman C, Paillere H, Vierendeels J, Dick E, Becker R, Braack M, Locke J. Modelling of natural convection flows with large temperature differences: a benchmark problem for low Mach number solvers. Part 1: reference solutions. *ESAIM. Math Model Numer Anal* 2005;39(3):609–16. doi: <https://doi.org/10.1051/m2an:2005027>.
- [32] Mavriplis DJ, Jameson A. Multigrid solution of the Navier-Stokes equations on triangular meshes. *AIAA J* 1990;28(8):1415–24. doi: <https://doi.org/10.2514/3.25233>.



Md Mizanur Rahman: Ph.D., Professor of Computational Fluid Dynamics (CFD) at Hangzhou Dianzi University since 2018. Worked at Aalto University in Finland for more than 20 years. Published 100 + papers, many of them are indexed by web of science.



Wenchang Liu: M.Sc. student in Hangzhou Dianzi University. CFD is his major subject.



Ming LV: Ph.D., Associate Professor of Mechanical Engineering at Hangzhou Dianzi University in China. Her research interests include CFD, renewable energy, thermo-fluid. She has published 10 scientific papers.



Huachen Pan: Ph.D., Professor of CFD at Hangzhou Dianzi University. Around 30 papers have been published, many of them are indexed by Web of Science or Engineering Index.